

Green Chemistry Letters and Reviews

ISSN: (Print) (Online) Journal homepage: https://www.tandfonline.com/loi/tgcl20

Molecular adsorption by biochar produced by eco-friendly low-temperature carbonization investigated using graphene structural reconfigurations

Kiminori Sato, Akinori Yamamoto, Michael Dyballa & Michael Hunger

To cite this article: Kiminori Sato, Akinori Yamamoto, Michael Dyballa & Michael Hunger (2022) Molecular adsorption by biochar produced by eco-friendly low-temperature carbonization investigated using graphene structural reconfigurations, Green Chemistry Letters and Reviews, 15:1, 287-295, DOI: 10.1080/17518253.2022.2048090

To link to this article: https://doi.org/10.1080/17518253.2022.2048090

© 2022 The Author(s). Published by Informa UK Limited, trading as Taylor & Francis Group

Published online: 07 Mar 2022.

Submit your article to this journal

Article views: 315

View related articles

View Crossmark data

Full Terms & Conditions of access and use can be found at
https://www.tandfonline.com/action/journalInformation?journalCode=tgcl20

GREEN CHEMISTRY LETTERS AND REVIEWS
2022, VOL. 15, NO. 1, 287–295
https://doi.org/10.1080/17518253.2022.2048090

Taylor & Francis
Taylor & Francis Group

LETTER

OPEN ACCESS Check for updates

Molecular adsorption by biochar produced by eco-friendly low-temperature carbonization investigated using graphene structural reconfigurations

Kiminori Sato [a], Akinori Yamamoto [a], Michael Dyballa [b] and Michael Hunger [b]

[a]Department of Environmental Sciences, Tokyo Gakugei University, Tokyo, Japan; [b]Institute of Technical Chemistry, University of Stuttgart, Stuttgart, Germany

ABSTRACT

Biochar is a promising material for environmental amendment. However, the adsorption mechanism of nitrogen-based ionic species, particularly the pH dependence, is still under debate because of its high susceptibility to experimental conditions. In this study, the adsorption of ammonium sulfate by rice-husk biochar produced by low-temperature carbonization as an eco-friendly approach was studied using Fourier-transform infrared (FT-IR) spectroscopy, ^{13}C magic-angle spinning (MAS) nuclear magnetic resonance (NMR), and open-space analysis using positrons coupled with molecular simulations. In the aqueous solution with pH of 5.38, graphenes are isolated exposing fresh surfaces, which physisorb NH_4^+ via interaction with π electrons rather than surface functional groups. Furthermore, the low-temperature carbonization leads to a lower degree of graphitization with grain boundary defects in graphene, triggering the fracture of graphene during the shaking process in an aqueous solution. SO_4^{2-} physisorption occurs as an outer-sphere surface complex on the positive charge caused by a charge transfer of ~2.5% from the terminal hydrogen at the graphene edge. A decrease in aqueous pH by ~0.7% significantly changes the above adsorption properties both on the surfaces and at the edges: diminishment of physisorption and transition to chemisorption by the formation of an inner-sphere surface complex.

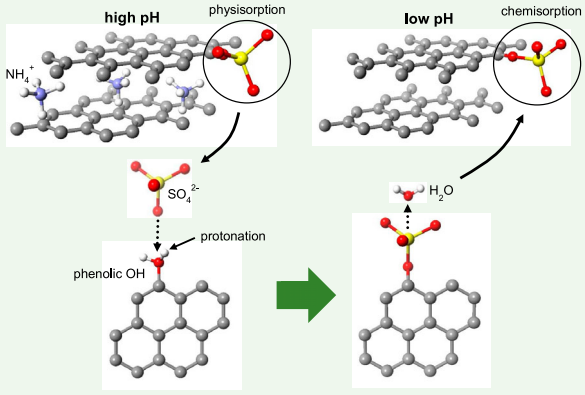

ARTICLE HISTORY
Received 22 November 2021
Accepted 24 February 2022

KEYWORDS
Biochar; graphene; structural reconfiguration; molecular adsorption; eco-friendly production

1. Introduction

Owing to the potential for soil amendment, water pollution control, crop production, and greenhouse gas reduction, biochar has been a promising candidate for environmental application (*1*). Particularly, thermochemical processes as low-temperature carbonization have recently attracted attention as one of the eco-friendly approaches for synthesis of solid biochar (*2*). Sorption experiments for nitrogen- and sulfur-based species using batch equilibration have yielded satisfactory performances in many cases (*3*). The high adsorption capability has been explained mainly through electrostatic and chemical interactions with charged functional groups on the surface of the biochar (*4, 5*). For example, oxygen functional groups with a negative charge exist on the biochar surfaces, which attract ammonium via electrostatic interaction enhancing the adsorption performance (*6*). FT-IR spectroscopy demonstrated -COOH, C=O, -OH, and other functional groups on the biochar surface (*2*). The adsorption capability in an aqueous solution often exhibits pH dependence. Generally, it is reduced at a low aqueous pH (*4*). The above tendencies are

CONTACT Kiminori Sato sato-k@u-gakugei.ac.jp Department of Environmental Sciences, Tokyo Gakugei University, 4-1-1 Koganei, Tokyo 184-8501, Japan

This article has been republished with minor changes. These changes do not impact the academic content of the article.

© 2022 The Author(s). Published by Informa UK Limited, trading as Taylor & Francis Group
This is an Open Access article distributed under the terms of the Creative Commons Attribution License (http://creativecommons.org/licenses/by/4.0/), which permits unrestricted use, distribution, and reproduction in any medium, provided the original work is properly cited.

sensitively influenced by ambient sample conditions (e.g. the origin of the feedstock and production history) (*7*).

Biochar, a carbonaceous organic matter produced from the pyrolysis of biomass feedstocks under oxygen-free or limited conditions, is a type of graphite material (*1*). Thus, the minimum structural unit of biochar can be assumed to be graphene, a two-dimensional nanosheet consisting of sp^2-hybridized carbon atoms with covalent bonds in a hexagonal honeycomb structure (*8*). In contrast to the in-plane covalent bonding, graphene nanosheets are weakly stacked by van der Waals forces. Hence, graphite can be easily exfoliated into graphenes, as initiated in the study on graphene isolation with Scotch tape (*9*). Nanotechnologically, the graphite exfoliation in an aqueous solution is a well-known approach for a large mass production of single- and few-layer graphene nanosheets (*10*). In practical biochar applications, the particular conditions involved in molecular adsorption are similar to those of graphite exfoliation in an aqueous solution (i.e. wet conditions). Thus, biochar applications involve isolation of graphene, exposure of fresh surfaces to a solution, and reconfiguration.

In this study, the molecular adsorption of ammonium sulfate by a rice-husk biochar produced by a low-temperature carbonization was investigated, focusing on the structural reconfigurations of graphene following isolation in an aqueous solution. We attempted to identify the local structural disorder caused by adsorption-dependent graphene reconfigurations, for example, a nanovoid among the graphite particles. Conventional diffraction and scattering techniques, such as high-resolution transmission electron microscopy, cannot be easily applied to probe the structural and electronic states of the above local disorders. Thus, we employed a positron annihilation technique, which is powerful to study various local disorders such as vacancy (*11*), grain boundary (*12, 13*), polar element (*14, 15*), local space charge (*16*), nanoprecipitate (*17*), and local glassy disorder (*18*) as well as angstrom-scale open spaces formed by clay nanosheet overlap (*19, 20*). It is found that graphene reconfigurations influenced by molecular adsorption both on the surfaces and at the edges can be studied by positrons. The emergence and inhibition of molecular adsorption on graphene surfaces perceptive to a aqueous pH are elucidated along with the transition of adsorption properties at graphene edges.

2. Experimental

2.1. Materials

The feedstock of the present biochar is rice husk available as an agricultural waste, supplied by a farmer in the Tsukuba area, Japan. A rice-husk-based biochar was produced by the thermal decomposition of rice husk mounds using a hood and chimney on site, where the pyrolysis temperature was low, at approximately 400°C. Two types of nitrogen stock solution were prepared by dissolving ammonium sulfate in ultrapure water. The aqueous pH values measured by an electrode-type pH meter (model FE20, Mettler Toledo AG) were 5.31 and 5.38. 0.2 g of the biochar sample was added to 50 mL of the above nitrogen stock solution. Each mixture was shaken in a thermostatic shaker at 25°C and 200 rpm for 24 h to achieve equilibrium. Thereafter, the mixtures were passed through a filter paper (type 5C, ADVANTEC). The samples were fully dried in an oven and subjected to FT-IR spectroscopy, ^{13}C MAS NMR, and positron lifetime spectroscopy.

2.2. FT-IR spectroscopy

Attenuated total reflection (ATR) FT-IR spectra were measured using a FT-IR spectrometer (Nicolet iS5, Thermo Fisher Scientific Inc.) equipped with an ATR device and diamond crystal plate. All FT-IR spectra were measured at room temperature with a resolution of 4 cm^{-1}. The measurements were repeated 20 times. The final spectra were obtained by averaging them. The software OMNIC 8.2 was used to display absorbance spectra by converting ATR data, where the absorption band at wavenumbers around 1000 cm^{-1} was focused.

2.3. Solid-state NMR

^{13}C MAS NMR experiments were performed using a Bruker Avance III 400WB spectrometer at a resonance frequency of 100.6 MHz. ^{13}C MAS NMR spectra were recorded by exciting the ^{13}C spins with single-pulses of 2.0 μs, ^{1}H decoupling, and repetition time of 20 s, thus avoiding the relaxation effects of T_1. The sample spinning rate was 8 kHz; 320 scans were collected for each spectrum. The chemical shifts of the ^{13}C nuclei in the adsorbed organic species were determined with respect to tetramethylsilane as an external reference, with an accuracy of ±1 ppm.

2.4. Positron lifetime spectroscopy

The graphene reconfigurations influenced by molecular adsorption were investigated by positron lifetime spectroscopy using a digital oscilloscope (WaveSurfer 10, Teledyne LeCroy) (*21*). The positron source (^{22}Na), sealed in a thin foil of Kapton, was mounted in a sample-source-sample sandwich configuration. The 1.27-MeV positron

birth γ-ray from a ^{22}Na source and one of the 511-keV γ-rays emitted as a result of positron annihilation in the samples were detected by BaF_2 scintillators with dimensions of 1″ (diameter) × 1″ (thickness) coupled with photomultiplier tubes (H3378-51, HAMAMATSU). Positron lifetime spectra (~1×10^6 coincidence counts) were recorded at room temperature. The time resolution of the present system was ~200 ps (full-width at half-maximum). The positron lifetime spectra were numerically analyzed after subtraction of the background.

2.5. Molecular simulations

The local molecular structure of a sulfate ion SO_4^{2-} absorbed at the graphene edges was optimized by molecular orbital (MO) calculations using molecular mechanics (MM3) in SCIGRESS 2.8 (Fujitsu Ltd.). Details have been presented elsewhere (*22–24*). In addition, a discrete variational (DV)-*Xα* MO calculation using the SCAT program (*25*) was carried out for the six-fold-graphene ring system including a carbon atom terminated by hydrogen. The net charge around the carbon atom and bond overlap population between the carbon and terminal hydrogen atoms were obtained. In the present calculations, the exchange scaling parameter *R* in the Slater's exchange potential was fixed to be 0.70 for all atoms (*26*, *27*). An approach using the above DV-*Xα* method is described in detail elsewhere (*25*).

3. Results and discussion

Figure 1 shows the results of FT-IR spectroscopy for a (a) pure $(NH_4)_2SO_4$, (b) pristine biochar, and biochar treated with $(NH_4)_2SO_4$ solutions with pH of 5.38 and 5.31. In accordance with the literature (*28*), the spectrum of the pure $(NH_4)_2SO_4$ exhibits intense peaks at wavenumbers of ~1050 cm^{-1} and ~1400 cm^{-1}, originating from the asymmetric S-O stretching vibration in SO_4^{2-} (gray arrow) and N-H bending vibration in NH_4^+ (black arrow), respectively. Three broad humps caused by overlapping of the N-H stretching mode can be additionally observed at 2800–3300 cm^{-1} (black arrows) (*28*). Absorption bands characteristic for graphite materials are observed at ~1080 cm^{-1} and ~1600 cm^{-1} for the pristine biochar, resulting from the stretching vibration of C–O-C in the epoxy group and stretching vibration of C=C in the aromatic ring, respectively (*29*). Furthermore, a broad band appears at ~3400 cm^{-1}, which can be attributed to a phenolic OH group with hydrogen bonding, marked by a gray circle (*30*). For the pH-5.38 $(NH_4)_2SO_4$ solution-treated sample, peaks at ~1050 cm^{-1} and ~1400 cm^{-1} as well as three humps at 2800–3300 cm^{-1} emerge (black and gray arrows).

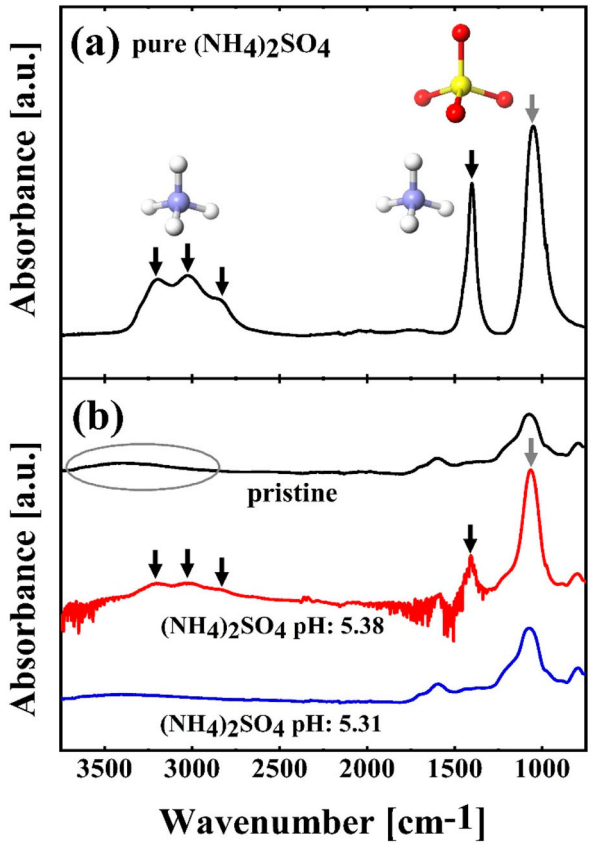

Figure 1. FT-IR spectra for the (a) pure $(NH_4)_2$, (b) pristine biochar, and biochar treated with $(NH_4)_2SO_4$ solutions with pH of 5.38 and 5.31. Adsorption peaks originating from NH_4^+ and SO_4^2 are indicated by black and gray arrows, respectively. The broad band attributed to a phenolic OH group with hydrogen bonding is marked by a gray circle. Schematics of NH_4^+ and SO_4^2 are shown as insets. The white, blue, red, and yellow objects correspond to proton, nitrogen, oxygen, and sulfur, respectively.

This demonstrates that SO_4^{2-} and NH_4^+ dissociated in the $(NH_4)_2SO_4$ solution were adsorbed by the biochar. On the contrary, the FT-IR spectrum observed for the pH-5.31 solution-treated sample is similar to that of the pristine biochar: the bands of SO_4^{2-} and NH_4^+ are not observed.

A graphene lattice with aromatic chemical compounds possesses π electrons delocalizing out of the basal plane, in contrast to in-plane covalent σ bonds owing to sp^2 hybridization. This suggests that π electrons on the surface of graphene are candidates for adsorption of NH_4^+ through physisorption. On the other hand, SO_4^{2-} is adsorbed on a local molecular site and is positively charged. The sulfate ion in an aqueous solution is a tetrahedral molecule with a higher symmetry, where a single peak appears around 1100 cm^{-1} due to the triplydegenerated ν_3 band (*31*). If sulfate ions are immobile as inner-sphere complexes,

their symmetry is reduced, leading to the splitting of the v_3 band. The symmetry of the outer-sphere complex without any chemical bonds would be similar to that of SO_4^{2-} in an aqueous solution, exhibiting a single peak. Thus, we infer that SO_4^{2-} adsorbs on the biochar sample, forming an outer-sphere complex without chemical bonds. By theoretical calculations, it has been predicted that graphene edges are terminated with hydrogen atoms in a stable manner because of the reduction in edge energy (*32*). The quantitative analysis of the overlap population based on the present DV-*Xα* calculation for six-fold-graphene with terminal hydrogen indicates that the attachment of protons to the graphene edge causes a charge transfer of ~2.5% to carbon atoms. This causes an effective positive charge on the graphene edge, attracting SO_4^{2-} as the outer-sphere complex through Coulombic interactions.

Figure 2 shows ^{13}C MAS NMR spectra for the pristine biochar (black) and biochar treated with $(NH_4)_2SO_4$ solutions with pH of 5.38 (red) and 5.31 (blue). The spectrum of the pristine biochar sample exhibited an intense signal and broad hump at chemical shifts of approximately 130 and 25 ppm, respectively. They originate from the carbon atoms of aromatic rings and aliphatic unincorporated into the aromatic skeleton, which is typically observed for graphite materials (*33*). The spectrum remains unchanged for the biochar sample treated with the $(NH_4)_2SO_4$ solution at pH of 5.38. Upon the decrease in the pH to 5.31, small signals appeared at chemical shifts of approximately 75 and 55 ppm, as indicated by the arrows. The appearance of these small signals implies that a small fraction of SO_4^{2-} is chemisorbed in the form of C-SO_4-H with a single C–O bridge at the edge site of graphene, as shown in the MO-optimized structure of SO_4^{2-} on the right-hand side of Figure 2. The broad adsorption band of the phenolic OH group with hydrogen bonding was observed in the FT-IR spectrum of the pristine biochar sample (gray circle in Figure 2 (b)). Thus, we propose the following scenario: SO_4^{2-} chemisorption with a single C–O bridge is caused by the formation of an inner-sphere surface complex involving ligand exchange with the phenolic OH group (see Figure 3). The phenolic OH group located at the graphene edge is protonated under a low aqueous pH, by which SO_4^{2-} is replaced with OH, releasing H_2O based on the reaction $COH + H^+ + SO_4^{2-} \rightarrow COSO_3^- + H_2O$.

Table 1 lists the positron lifetimes observed for (a) kish graphite, (b) glassy carbon, (c) pristine biochar, and biochar treated with $(NH_4)_2SO_4$ solutions with pH of (d) 5.38 and (e) 5.31. Prior to the discussion of the results of positron lifetime spectroscopy, the possible positron annihilation sites in graphite are described. Positrons annihilate at the defect-free region and lattice vacancy in the graphite crystallites with positron lifetimes of ~ 220 ps and ~ 250 ps, respectively (see the upper left part of Figure 4) (*34*). The vacancy-type defect in the grain boundary, known as grain boundary

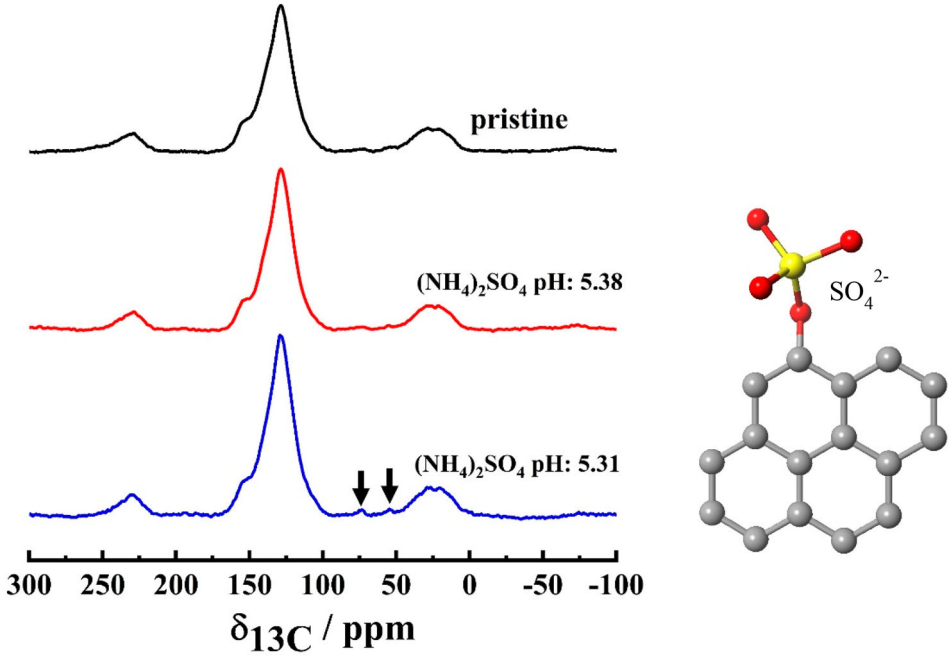

Figure 2. ^{13}C MAS NMR spectra for the pristine biochar (black) and biochar treated with $(NH_4)_2SO_4$ solutions with pH of 5.38 (red) and 5.31 (blue). Signals originating from SO_4^{2-} are indicated by arrows. The MO-optimized structure of SO_4^{2-} at the graphene edge is shown on the right-hand side. The gray red, and yellow objects correspond to carbon, oxygen, and sulfur, respectively.

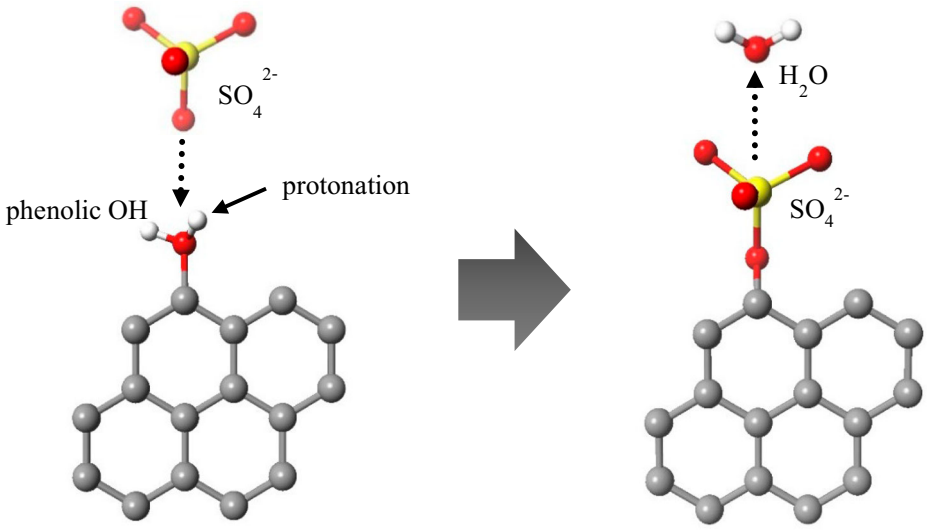

Figure 3. Schematics of chemisorption of SO_4^{2-} through ligand exchange at the edge site of graphene. The gray, red, white, and yellow objects correspond to carbon, oxygen, proton, and sulfur, respectively.

defect, resulting from the gathering of pentagon and heptagon, can also be a candidate for positron trapping (see the upper right part) (*35*). The positron lifetime therein could be similar to that of the lattice vacancy in the graphite crystallites because of the similar sizes. In addition, nanovoids among graphite particles have often been identified with a long component with a positron lifetime of ~400 ps, as illustrated in the bottom panel of Figure 4 (*34*).

The positron lifetime τ_1~219 ps in the defect-free region is exclusively observed for the kish graphite with a high crystallinity, similar to the single-crystalline graphite. The glassy carbon exhibits a longer positron lifetime of τ_2 ~387 ps corresponding to nanovoids among graphite particles due to turbostratic stacking (*36*). Positron lifetime spectroscopy for the pristine biochar yields two components with positron lifetimes of τ_1 ~251 ps and τ_2 ~384 ps with relative intensities of I_1 ~19% and I_2 ~81%, respectively. According to the comparison to the results of the kish graphite and glassy carbon as well as the above literature data, the positron lifetime τ_1 for the pristine biochar can be attributed to annihilation either at the lattice vacancies or grain boundary defects. The long component τ_2 originates from the annihilation in the nanovoids among the graphite particles. In contrast to the earlier results of positron lifetime spectroscopy for graphite (*34*), a defect-free region was not observed for the pristine biochar sample. We expect that the biochar sample prepared by the low-temperature carbonization is defective with a lower degree of graphitization, as often observed for other carbon materials (*37*).

For the biochar sample treated with the $(NH_4)_2SO_4$ solution at pH of 5.38, positron lifetimes of τ_1 ~217 ps and τ_2 ~364 ps were obtained with relative intensities of I_1 ~65% and I_2 ~35%, respectively. The positron lifetime τ_1 is significantly shorter than that of the pristine biochar and is close to that of the kish graphite, where the positron lifetime of τ_1 ~213 ps in the defect-free region is exclusively observed. Thus, the positron lifetime τ_1 for the pH-5.38 $(NH_4)_2SO_4$ solution-treated biochar corresponds to annihilation in the defect-free region of the graphite crystallites. Notably, the lattice vacancies or grain boundary defects disappear and the

Table 1. Positron lifetimes τ_1 and τ_2 and their relative intensities I_1 and I_2 evaluated for (a) kish graphite, (b) glassy carbon, (c) pristine biochar, (d) biochar treated with the $(NH_4)_2SO_4$ solution with pH of 5.38, and (e) biochar treated with the $(NH_4)_2SO_4$ solution with pH of 5.31. Positron annihilation sites 1 and 2 corresponding to positron lifetimes τ_1 and τ_2 are also presented.

Sample	τ_1 [Å]	site 1	I_1 [%]	τ_2 [Å]	site 2	I_2 [%]
(a) Kish graphite	219 ± 3	Defect-free region	100	–	–	0
(b) Glassy carbon	–	–	0	387 ± 5	Nanovoid	100
(c) Pristine biochar	251 ± 3	Vacancy-type defect	19 ± 2	384 ± 5	Nanovoid	81 ± 3
(d) Biochar treated with pH 5.38 solution	217 ± 3	Defect-free region	65 ± 2	364 ± 4	Nanovoid	35 ± 2
(e) Biochar treated with pH 5.31 solution	–	–	0	374 ± 5	Nanovoid	100

defect-free region alternatively appears upon treatment with an aqueous solution. This can be explained by the presence of grain boundary defects rather than the lattice vacancies. According to the analysis of mechanical properties using molecular dynamics simulation, the vacancy-type defect at the grain boundary is the initial failure site leading to brittle cracks (*38*). It is reasonable to infer that the grain boundary defects probed by positrons trigger a fracture of graphene during the shaking in an aqueous solution and disappear. The positron lifetime τ_2 is similar to that of the longer positron lifetime observed for the pristine biochar, and is thus attributed to nanovoids among the graphite particles. At the low aqueous pH of 5.31, the shorter positron lifetime attributed to the defect-free region in the graphite crystallites disappears; i.e. a positron lifetime τ_2 of 374 ps associated with nanovoids among graphite particles is exclusively obtained.

As mentioned above, graphenes in graphite materials are weakly bound by van der Waals forces between adjacent layers (*9*). Ionic molecules such as NH_4^+ can penetrate into the interlayer spaces between graphene nanosheets in an aqueous solution and can easily separate them from graphite materials, which has been utilized for graphite exfoliation in the electrochemical process (*10*). It is presumed that a fraction of graphene nanosheets is isolated in the $(NH_4)_2SO_4$ aqueous solution, as illustrated in the bottom panel of Figure 4. The appearance of a ~65% defect-free region for the pH-5.38 $(NH_4)_2SO_4$ solution-treated sample indicates that the graphene nanosheets are tightly recompressed as graphite crystallites. On the contrary, the disappearance of the defect-free region and alternative appearance of nanovoids for the pH-5.31 $(NH_4)_2SO_4$ solution-treated sample are result of the imperfect restacking of graphenes (see the schematic in the bottom panel of Figure 4). Similar tendencies have been observed for clay nanoparticles, where the structural reconfigurations of nanosheet arrays are influenced by solution concentration (*39–41*).

Based on the findings obtained by the FT-IR spectroscopy, ^{13}C MAS NMR, and positron lifetime spectroscopy together with molecular simulations, the following mechanism can be proposed for the pH-dependent adsorption of ammonium sulfate by the present rice-husk biochar. Graphenes weakly bound by van der Waals forces between adjacent layers are isolated in aqueous solutions, exposing fresh surfaces with fewer functional groups. Thus, the electrostatic interaction with π electrons on the graphene surface is responsible for the adsorption of NH_4^+ at pH of 5.38. The physisorption of NH_4^+ on the graphene surfaces increases the width of the electrical double layer around graphenes (*42*), weakening the van der Waals forces between the adjacent layers. Thereby, the agglomeration of graphenes is suppressed in the

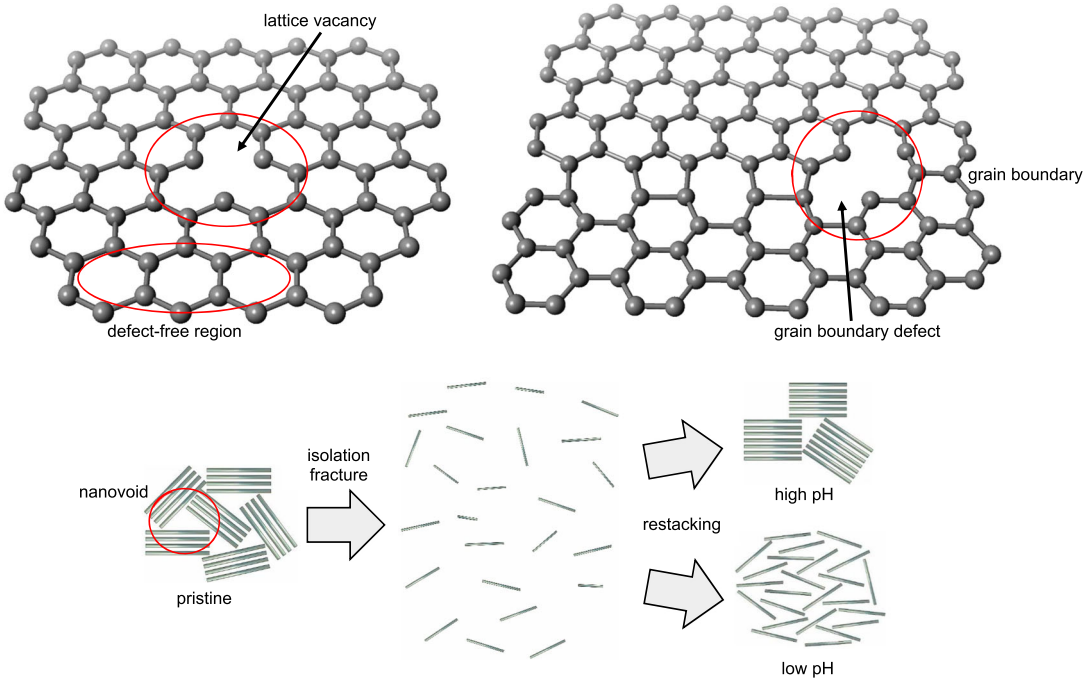

Figure 4. Schematics of possible positron annihilation sites: defect-free region, lattice vacancy, grain boundary defect, and nanovoid, and graphene isolation in the aqueous solution and restacking under the conditions under a high pH and low pH.

process of restacking in an aqueous solution, being tightly recompressed as kish graphite (see Table 1). Parts of graphene edges also appear in the aqueous solution owing to the isolation and fracture of graphene, which are instantaneously terminated with hydrogen. Charge transfer occurs from the terminated hydrogen to aromatic carbon, by which the graphene edge is positively charged attracting SO_4^{2-} as an outer-sphere surface complex via Coulombic interactions.

At pH of 5.31, mobile protons that are more abundantly available in the aqueous solution preferentially attach to the surface of the graphene nanosheet hindering the adsorption of NH_4^+. The attachment of protons on graphene surfaces does not significantly vary the width of the electrical double layer around the nanosheet, triggering the agglomeration of graphenes with nanovoids as glassy carbon (see Table 1). In this agglomeration, the graphene edges further appear along with phenolic OH to be protonated. Negative sulfate species are electrostatically attracted by the protonated phenolic OH located at the graphene edges. The interaction between SO_4^{2-} and protonated phenolic OH could thus be effective in comparison to the local positive charge of ~2.5% on the graphene edge induced by charge transfer. Therefore, the adsorption of SO_4^{2-} at the graphene edges changes from physisorption as an outer-sphere surface complex to chemisorption via the formation of an inner-sphere surface complex involving ligand exchange.

We discuss the origin of the inhibition of adsorption capability upon a slight decrease in pH by ~0.7% for the rice-husk-based biochar employed in this study. In our earlier studies on boric acid adsorption by light-burned MgO (*43*), protons in the aqueous solution were concentrated at the broken bonds on the interior surfaces of the open spaces. The surface of graphene could not be atomically cleaned with coordinatively unsaturated carbon atoms as the interior surfaces of the light-burned MgO. The studied biochar sample was produced by pyrolyzing a large amount of rice husk at a relatively low carbonization temperature. The low-temperature carbonization processes may leave the above structural imperfections on the graphene surfaces, as evidenced by the presence of grain boundary defects in the graphite crystallites (see Table 1). Presumably, it is difficult to eliminate the local structural imperfections from the present rice-husk biochar, as suggested by the reactive open-space surfaces in amorphous silica produced by rice husks (*44, 45*). Such local structural imperfections, originating from feedstock and/or production history, could contribute to a strong proton accumulation, even with a decrease of ~0.7% in the aqueous pH.

4. Conclusion

The molecular mechanism of the adsorption of ammonium sulfate by rice-husk-based biochar produced by the eco-friendly low-temperature carbonization was studied by FT-IR spectroscopy, ^{13}C MAS NMR, and open-space analysis using positrons coupled with molecular simulations. In the $(NH_4)_2SO_4$ aqueous solution, graphene was isolated, exposing fresh surfaces, and then reconfigurated under the influence of the aqueous pH. A significant amount of NH_4^+ adsorbed on the graphene surfaces through electrostatic interactions with π electrons rather than functional surface groups at pH of 5.38. Furthermore, SO_4^{2-} physisorbs acted as outer-sphere surface complexes on the local positive charges located at the graphene edges. In response to the decrease in aqueous pH of ~0.7%, mobile protons that were more abundantly available in the solution transiently attached to the graphene surfaces, interrupting the physisorption of NH_4^+ The above SO_4^{2-} physisorption at the graphene edges changed to chemisorption by the formation of an inner-sphere surface complex involving ligand exchange. The inhibition of the adsorption capability of graphene surfaces should be considered when low-temperature carbonization is involved in biochar production as a sustainable and eco-friendly approach.

Disclosure statement

No potential conflict of interest was reported by the author(s).

Funding

This work was partially supported by Grants-in-Aid of the Ministry of Education, Culture, Sports, Science and Technology of Japan; JSPS [grant numbers 20K14372, and 21K20352].

ORCID

Kiminori Sato http://orcid.org/0000-0002-1622-5293
Akinori Yamamoto http://orcid.org/0000-0002-1308-3904
Michael Dyballa http://orcid.org/0000-0002-8883-1145
Michael Hunger http://orcid.org/0000-0002-1870-2743

References

[1] Hagemann, N.; Joseph, S.; Schmidt, H.P.; Kammann, C.I.; Harter, J.; Borch, T.; Young, R.B.; Varga, K.; Taherymoosavi, S.; Elliott, K.W.; McKenna, A.; Albu, M.; Mayrhofer, C.; Obst, M.; Conte, P.; Alonso, A.D.; Orsetti, S.; Subdiaga, E.; Behrens, S.; Kappler, A. Organic Coating on Biochar Explains its Nutrient Retention and Stimulation of Soil Fertility. *Nat. Commun.* **2017,** *8*, 1089.
[2] Itoh, T.; Iwabuchi, K.; Maemoku, N.; Sasaki, I.; Taniguro, K. A new Torrefaction System Employing Spontaneous Self-

Heating of Livestock Manure Under Elevated Pressure. *Waste Manage.* **2019,** *85*, 66–72.
[3] Cai, Y.; Qi, H.; Liu, Y.; He, X. Sorption/desorption behavior and mechanism of NH4 + by biochar as a nitrogen fertilizer sustained-release material. *J. Agric. Food Chem.* **2016,** *64* (24), 4958–4964.
[4] Fidel, R.B.; Laird, D.A.; Spokas, K.A. Sorption of Ammonium and Nitrate to Biochars is Electrostatic and pH-Dependent. *Sci. Rep.* **2018,** *8*, 17627.
[5] Kizito, S.; Wu, S.; Kirui, W.K.; Lei, M.; Lua, Q.; Baha, H.; Donga, R. Evaluation of Slow Pyrolyzed Wood and Rice Husks Biochar for Adsorption of Ammonium Nitrogen from Piggery Manure Anaerobic Digestate Slurry. *Sci. Total Environ.* **2015,** *505*, 102–112.
[6] Gao, F.; Xue, Y.; Deng, P.; Cheng, X.; Yang, K. Removal of Aqueous Ammonium by Biochars Derived from Agricultural Residuals at Different Pyrolysis Temperatures. *Chem. Speciation Bioavailability* **2015,** *27*, 92–97.
[7] Takaya, C.A.; Fletcher, L.A.; Singh, S.; Anyikude, K.U.; Ross, A.B. Phosphate and Ammonium Sorption Capacity of Biochar and Hydrochar from Different Wastes. *Chemosphere* **2016,** *145*, 518–527.
[8] Geim, A.K.; Novoselov, K.S. The Rise of Graphene. *Nat. Mater.* **2007,** *6*, 183–191.
[9] Novoselov, K.S.; Geim, A.K.; Morozov, S.V.; Jiang, D.; Zhang, Y.; Dubonos, S.V.; Grigorieva, I.V.; Firsov, A.A. Electric Field Effect in Atomically Thin Carbon Films. *Science* **2004,** *306*, 666–669.
[10] Parvez, K.; Wu, Z.S.; Li, R.; Liu, X.; Graf, R.; Feng, X.; Müllen, K. Exfoliation of Graphite Into Graphene in Aqueous Solutions of Inorganic Salts. *J. Am. Chem. Soc.* **2014,** *136*, 6083–6091.
[11] Sato, K.; Baier, F.; Rempel, A.A.; Sprengel, W.; Schaefer, H.-E. Observation of High-Temperature Thermal Vacancies in Quasicrystals. *Phys. Rev. B* **2003,** *68*, 214203.
[12] Li, W.; Li, X.; Guo, D.; Sato, K.; Gunderov, D.V.; Stolyarov, V.V.; Zhang, X. Atomic-scale Structural Evolution in Amorphous Nd9Fe85B6 Subjected to Severe Plastic Deformation at Room Temperature. *Appl. Phys. Lett.* **2009,** *94*, 231904.
[13] Sato, K. Grain-boundary Structures Associated with Ionic Transport in Gd-Doped Ceria Nanostructured Electrolyte. *J. Phys. Chem. C* **2015,** *119*, 5734–5738.
[14] Sato, K.; Murakami, H.; Ito, K.; Hirata, K.; Kobayashi, Y. Probing the Elemental Environment Around the Free Volume in Polymers with Positron Annihilation Age −Momentum Correlation Spectroscopy. *Macromolecules* **2009,** *42*, 4853–4857.
[15] Sato, K. Study of Salt Precipitation in Polymer Electrolytes Based on Poly(Ethylene Oxide) and EMImTf Ionic Liquid. *J. Phys. Chem. B* **2018,** *122*, 7009–7014.
[16] Sato, K. Probing Charge-State Distribution at Grain Boundaries Varied with Dopant Concentration for Ceria Ceramics. *J. Phys. Chem. C* **2017,** *121*, 20407–20412.
[17] Yu, R.S.; Ito, K.; Hirata, K.; Sato, K.; Zheng, W.; Kobayashi, Y. Positron Annihilation Study of Defects and Si Nanoprecipitation in Sputter-Deposited Silicon Oxide Films. *Chem. Phys. Lett.* **2003**, *379*, 359–363.
[18] Sato, K.; Murakami, H.; Sprengel, W.; Schaefer, H.-E.; Kobayashi, Y. Nanocrystallization Mechanism of Amorphous Fe78B13Si9. *Appl. Phys. Lett.* **2009,** *94*, 171904.
[19] Sato, K.; Numata, K.; Dai, W.; Hunger, M. Long-term Self-Assembly of Inorganic Layered Materials Influenced by the Local States of the Interlayer Cations. *Phys. Chem. Chem. Phys.* **2014,** *16*, 10959–10964.
[20] Sato, K.; Numata, K.; Dai, W.; Hunger, M. Tunable States of Interlayer Cations in Two-dimensional Materials. *Appl. Phys. Lett.* **2014,** *104*, 131901.
[21] Sato, K.; Hunger, M. Carbon Dioxide Adsorption in Open Nanospaces Formed by Overlap of Saponite Clay Nanosheets. *Commun. Chem.* **2020,** *3*, 91.
[22] Alinger, N.L.; Yuh, Y.H.; Lii, J.-H. *J. Am. Chem. Soc.* **1989,** *111*, 8551–8566.
[23] Lii, J.-H.; Alinger, N.L. *J. Am. Chem. Soc.* **1989,** *111*, 8566–8575.
[24] Lii, J.-H.; Alinger, N.L. *J. Am. Chem. Soc.* **1989,** *111*, 8576–8582.
[25] Adachi, H.; Tsukada, M.; Satoko, C. Discrete Variational Xα Cluster Calculations. I. Application to Metal Clusters. *J. Phys. Soc. Jpn* **1978,** *45*, 875–883.
[26] Slater, J.C. A Simplification of the Hartree-Fock Method. *Phys. Rev.* **1951,** *81*, 385–390.
[27] Slater, J.C. Magnetic Effects and the Hartree-Fock Equation. *Phys. Rev.* **1951,** *82*, 538–541.
[28] Kadama, S.S.; Mesbaha, A.; van der Windt, E.; Kramer, H.J.M. Rapid Online Calibration for ATR-FTIR Spectroscopy During Batch Crystallization of Ammonium Sulphate in a Semi-Industrial Scale Crystallizer. *Chem. Eng. Res. Des.* **2011,** *89*, 995–1005.
[29] Li, G.; Zhu, W.; Zhu, L.; Chai, X. Effect of Pyrolytic Temperature on the Adsorptive Removal of p-Benzoquinone, Tetracycline, and Polyvinyl Alcohol by the Biochars from Sugarcane Bagasse. *Korean J. Chem. Eng.* **2016,** *33*, 2215–2221.
[30] Mikhaylova, Y.; Adam, G.; Häussler, L.; Eichhorn, K.-J.; Voit, B. Temperature-dependent FTIR Spectroscopic and Thermoanalytic Studies of Hydrogen Bonding of Hydroxyl (Phenolic Group) Terminated Hyperbranched Aromatic Polyesters. *J. Mol. Struct.* **2006,** *788*, 80–88.
[31] Persson, P.; Lovgren, L. Potentiometric and Spectroscopic Studies of Sulfate Complexation at the Goethite-Water Interface. *Cosmochim. Acta.* **1996,** *60*, 2789–2799.
[32] He, K.; Lee, G.D.; Robertson, A.W.; Yoon, E.; Warner, J.H. Hydrogen-free Graphene Edges. *Nat. Commun.* **2014,** *5*, 3040.
[33] Zhao, Y.C.; Zhao, L.; Maoa, L.J.; Han, B.H. One-step Solvothermal Carbonization to Microporous Carbon Materials Derived from Cyclodextrins. *J. Mater. Chem. A* **2013,** *1*, 9456–9461.
[34] Shimotomai, M.; Iwata, T.; Takahashi, T.; Doyama, M. Vacancy in Graphite: Positron Srudies. *J. Phys. Soc. Jpn* **1983,** *52*, 694–702.
[35] Li, Z.L.; Li, Z.M.; Cao, H.Y.; Yang, J.H.; Shu, Q.; Zhang, Y.Y.; Xiang, H.J.; Gong, X.G. What are Grain Boundary Structures in Graphene? *Nanoscale.* **2014,** *6*, 4309–4315.
[36] Hasegawa, M.; Kajino, M.; Kuwahara, H.; Kuramoto, E.; Takenaka, M.; Yamaguchi, S. Irradiation-induced Defects in Graphite and Glassy Carbon Studied by Positron Annihilation. *Mater. Sci. Forum* **1992**, *105-110*, 1041–1046.
[37] Maruyama, J.; Maruyama, S.; Fukuhara, T.; Chashiro, K.; Uyama, H. Ordered Mesoporous Structure by Graphitized Carbon Nanowall Assembly. *Carbon. N. Y.* **2018,** *126*, 452–455.

[38] Yang, B.; Wang, S.; Guo, Y.; Yuan, J.; Si, Y.; Zhanga, S.; Chen, H. Strength and Failure Behavior of a Graphene Sheet Containing bi-Grain-Boundaries. *RSC Adv*. **2014,** *4*, 54677–54683.

[39] Sato, K.; Fujimoto, K.; Dai, W.; Hunger, M. Quantitative Elucidation of Cs Adsorption Sites in Clays: Toward Sophisticated Decontamination of Radioactive Cs. *J. Phys. Chem. C* **2016,** *120*, 1270–1274.

[40] Sato, K.; Hunger, M. Molecular Studies of Cs Adsorption Sites in Inorganic Layered Materials: The Influence of Solution Concentration. *Phys. Chem. Chem. Phys.* **2017,** *19*, 18481–18486.

[41] Sato, K.; Zhao, Y.; Kamaya, M. Structural Reconfigurations of Nanosheet Arrays in Layered Minerals Caused by Wave Irradiation: Desorption Mechanism of Cs from Nanosheet Edges. *Chem. Phys. Phys. Chem.* **2019,** *21*, 16345–16352.

[42] Jurado, L. A., Marzal, R. M. E. Insight Into the Electrical Double Layer of an Ionic Liquid on Graphene. *Sci. Rep.* **2017**, *7*, 4225.

[43] Sato, K.; Kamaya, M. Origin of Enhanced Boric Acid Adsorption in Light-Burned Magnesium Oxide. *J. Chem. Phys.* **2020,** *153*, 124704.

[44] Sato, K.; Fujimoto, K.; Nakata, M.; Hatta, T. Diffusion-reaction of Water Molecules in Angstrom Pores as Basic Mechanism of Biogenic Quartz Formation. *J. Phys. Chem. C* **2011,** *115*, 18131–18135.

[45] Sato, K. Origin of Organism-Dependent Biogenic Silica Quartz Formation. *J. Phys. Chem. B* **2011**, 115, 14874–14877.